International Journal of Hyperthermia

http://informahealthcare.com/hth
ISSN: 0265-6736 (print), 1464-5157 (electronic)

Int J Hyperthermia, 2013; 29(3): 169–180

DOI: 10.3109/02656736.2013.784813

informa healthcare

RESEARCH ARTICLE

Figures of merit and their bounds in radiofrequency heating by phased arrays

Fernando Bardati[1] & Piero Tognolatti[2]

[1]Department of Civil Engineering and Computer Science, University of Rome Tor Vergata, Rome, Italy and [2]Department of Industrial and Information Engineering, University of L'Aquila, L'Aquila, Italy

Abstract

Purpose: The problem of effective power delivery to a semi-deep target by a phased array has been addressed for application to hyperthermia treatment of some tumours in the thorax.
Methods: Three efficiencies have been introduced, which estimate system ability in power transfer from generators to body, from body to tumour, and from generators to tumour. They are formulated in terms of a dissipation matrix and an interference matrix. Bounds to achievable efficiencies are obtained. Further figures of merit have also been introduced. The necessary mathematics has been developed.
Results: A numerical analysis has been carried out for a partially interdigitated planar array of resonant dipoles. Results show how the new parameters can be exploited for optimal selection of the array's degrees of freedom.
Conclusion: The figures of merit and their bounds allow comparisons between RF heating devices and provide guidelines to phased array design.

Keywords

Local hyperthermia, phased array, RF heating

History

Received 24 July 2012
Revised 17 January 2013
Accepted 7 March 2013
Published online 16 April 2013

Introduction

Clinical trials have shown that the addition of hyperthermia to radiotherapy or chemotherapy results in improved clinical outcome [1–5]. There is general consensus that effectiveness of hyperthermia technology is a prerequisite for clinical effectiveness. The power distribution in the patient and the amount of power deposited in the tumour depend on the focusing capability of the hyperthermia device and on the ability to restrain hot spots in normal tissues [6]. For a given heating system the patient-specific anatomy has great influence on local power distribution, while the thermal properties of tissues and perfusion have a major impact on the resulting temperature distribution [7].

Radiating systems that have been proposed and are currently used to heat deep-seated tumours include phased arrays, where focusing onto targets can be obtained by constructive interference of the electromagnetic fields that are radiated by a set of applicators. The most popular phased array systems for regional hyperthermia of deep-seated tumours mainly located in the abdomen and pelvis are the BSD-1000 and BSD-2000 with Sigma applicators [8–10]. Other phased array systems are the AMC 4-waveguide applicator [11], recently upgraded to a new 8-waveguide system [12], the WACOA system [13] and the HYPERcollar [14]. The last device has been designed for local treatment of head and neck tumours. Focusing is obtained by selection of amplitude and phase in input at each applicator. Various optimisation procedures have been proposed which substantially differ in the choice of an appropriate objective function for evaluating the therapeutic quality of a certain selection, i.e. the quantitative assessment of treatment effects in terms of temperature related to major limiting side effects such as systemic stress (deposited power) and maximal temperatures in normal tissues, with possible hot spot generation [15–18]. However, local heating of some tumours cannot be performed by the above systems to a satisfactory degree.

An array of M elementary antennas is used whenever a deep tumour cannot be locally heated by a single antenna without excessive overheating of interposed tissue, so that its aggression from multiple directions is necessary also to improve power uniformity within the target. Phased arrays allow coherent operation with a gain up to M in comparison with the incoherent modality. Moreover, a phased array has some steering capability of the deposited power pattern by proper selection of amplitudes and phases of feed voltages. Steering may help to reduce hot spots in normal tissue. Finally, an operator can exploit the available degrees of freedom to deliberately defocus the array tailoring the power deposition pattern to meet constraints on induced temperature [19].

Number, spatial arrangement and operation frequency of antennas are important in array design for different tumours and sites [15,20–25]. In this paper a new approach is

Correspondence: Fernando Bardati, Department of Civil Engineering and Computer Science, University of Rome Tor Vergata, via del Politecnico 1, Roma 00133, Italy. Tel: +39-06-72597419. E-mail: bardati@disp.uniroma2.it

discussed, i.e. the array ability to deliver the largest fraction of available power from sources to a deep-seated tumour will be investigated using some efficiencies we introduce together with their bounds. Some additional figures of merit will also be considered. All these parameters can be used for comparisons among applicators and provide guidelines to array design. On the other hand, the selection of feed voltages for individual treatment optimisation is beyond the scope of this paper and will not be addressed.

Power deposition patterns depend on the operation frequency f. The choice of f is a trade-off between wave focusing and damping with distance. In this paper the ISM frequency in Europe of 434 MHz will be assumed, so that the side of a $40\,cm^3$ lesion is comparable with $\lambda_m/2$, where $\lambda_m = 8.8$ cm is the wavelength in a high-water-content tissue [26]. Phased array benefits from field interference from various sources. At 434 MHz the penetration depth is such that power reduces to 10% over a path length <6 cm in a muscle. Therefore, beneficial constructive interference for local heating is expected when the distance difference from interfering radiators to the target is not larger than a few centimetres, to be verified by full wave computations. For a semi-deep target in the thorax, abdomen or pelvis at 434 MHz, this is possible if the antennas are arranged on one side of the body, and they densely populate the array front towards the body.

Antennas have interfaces towards generators and body that rule power transfer to the target. These aspects will be considered in the next section, where efficiencies and other parameters will be introduced. Furthermore, a numerical analysis will be performed modelling a planar array of resonant dipoles as a benchmark. As a reference case we shall assume a target at 6–8 cm from the body surface. This may model a lung tumour. Both a skin–fat–muscle plane layering and a more realistic thorax phantom will be used in the numerical analysis. We shall use power loss instead of specific absorption rate (SAR) to model power delivery to tissues. Using power loss allows power transfer coefficients from sources to target to be written as pure numbers.

Methods

Power terms for efficiency evaluations

We shall introduce some efficiencies as ratios between powers we define hereafter. Let Ω be a body and ω a deep-seated target within the body. ω is heated by an array of antennas as a consequence of power deposition by the radiated electromagnetic field. M identical antennas are accomodated in front of the body (Figure 1) while their location and orientation are kept constant during a treatment. Each antenna is connected to a power source through a feed line, for example a coaxial cable of real-valued characteristic impedance R_0, while power sources are endowed with independent level and phase regulations [27]. The voltage of the source powering the mth antenna through its internal resistance R_0, is denoted by $V_{oc,m}$, i.e. the series of the open-circuit voltage $V_{oc,m}$ and R_0 is Thevenin's equivalent circuit of an M-channel RF generator evaluated at the mth antenna's terminals. $V_{oc,m}$ should not be confused with the voltage at the mth antenna's terminals. The relation between these voltages has been investigated in Nadobny et al. [28]. In particular, if even only one generator is fired, non-zero voltages appear at all antenna terminals which modify field and power patterns in Ω to some extent [29].

We assume that the lines are matched to the sources, as is common practice. On the other side there is normally a mismatch between lines and antennas with consequent power reflection. Furthermore, a fraction of the power entering the body from an antenna will be collected by the other antennas without heating the body. To take reflections and cross coupling among radiators into account, the body is modelled as a microwave junction whose M ports are the antenna terminals. a_m and b_m will denote the complex amplitude of the direct and reflected waves, respectively, so that $a_m a_m^*(b_m b_m^*)$ is the power carried by the direct (reflected) wave through port m, where an asterisk is for complex conjugate. Time dependence $e^{j2\pi ft}$ and phasor notation [30] are used throughout. Equation (1) transforms input variables from voltages to wave amplitudes.

$$[a] = [V_{oc}]/\sqrt{8R_0} \tag{1}$$

$[V_{oc}]$ is a column vector $[V_{oc,1}, V_{oc,2}, \ldots, V_{oc,M}]^T$, where T is for transposed, and similarly $[a]$. Small temperature changes have a negligible effect on tissue dielectric properties [31] so that the linearity hypothesis does not break down. Therefore, the amplitude of the waves reflected by the body is linearly related to the amplitude of the impinging waves by $[b] = [S][a]$, with $[S]$ an $M \times M$ complex-valued matrix. $[S]$ is known [32,33] as the scattering matrix for a junction. It is routinely measured by a vector network analyser. Guidelines for its computation can be found in Sadiku [34] and Taflove [35]. Furthermore, most commercial computer packages that are used for SAR calculations have an option for direct $[S]$ evaluation. Electromagnetic field reflections at the ports and cross coupling between ports are automatically accounted for by the on-diagonal and off-diagonal entries of $[S]$, respectively.

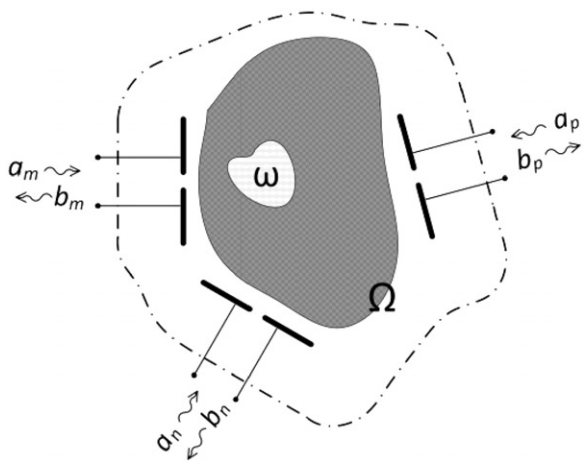

Figure 1. Array of antennas radiating onto a body Ω as a multiport microwave junction. ω is the target. Waves entering and leaving the junction are also shown.

The total available power, P_G, delivered by the generators to non-reflecting loads is obtained as the sum over the available power of each generator:

$$P_G = \sum_{m=1}^{M} a_m a_m^* = [a]^{T*}[a] \tag{2}$$

The total power, P_Ω, supplied to Ω through the M channels, is the difference between P_G and the power, $[b]^{T*}[b]$, which leaves the body after reflections (mismatches) and cross coupling, being finally absorbed by the internal resistance R_0 of the sources:

$$P_\Omega = [a]^{T*}[a] - [b]^{T*}[b] = [a]^{T*}[H][a] \tag{3}$$

A dissipation matrix [36], $[H] = [I] - [S]^{T*}[S]$, has been introduced in Equation (3), where $[I]$ is the identity matrix. $[a]^{T*}[H][a]$ is a quadratic Hermitian positive-definite form in $[a]$. The entries of $[H]$ are pure numbers with $H_{mm} < 1$ for any m.

It is worth working out an equation for P_Ω in terms of open circuit voltages which are more commonly employed in hyperthermia optimisation problems. It is also useful to refer these voltages to inputs which deliver a given amount of power to the body. The property of being dimensionless will be retained in the matrices we introduce. Accordingly $V_{oc,m}$ is written as in Equation (4).

$$V_{oc,m} = u_m \dot{V}_m \tag{4}$$

for $m = 1, \ldots, M$ with u_m a real-valued voltage following a suitable P_Ω normalisation reported in Appendix 1. $\dot{V}_m$ is a dimensionless complex factor, whose amplitude and phase are parameters left to individual treatment optimisation, which is not dealt with in this paper. From Equations (3) and (4) we obtain

$$P_\Omega = P_0 \left[\dot{V}\right]^{T*} [\bar{H}] \left[\dot{V}\right] \tag{5}$$

where $P_0 = 1$ watt is the reference power, $[\dot{V}]$ is the complex factor vector, and

$$\bar{H}_{mn} = H_{mn} / \sqrt{H_{mm} H_{nn}} \tag{6}$$

for any m and n. Later we shall use Equation (3) or (5) for P_Ω according to whether the input is modelled as waves $[a]$ or voltages $[\dot{V}]$. The change of variable from $[a]$ to $[\dot{V}]$ is given by

$$\left[\dot{V}\right] = P_0^{-1/2} [D]^{-1} [a] \tag{7}$$

where $[D]$ is defined in Appendix 1.

Finally, we model the power delivered to the target ω. Let the electric-field phasor at $\vec{r}$, a point of ω, be $\vec{e}_m$ when the mth generator open-circuit voltage is u_m while the remaining generators are switched off, i.e. $\dot{V}_n = \delta_{nm}$, $n = 1, \ldots, M$. δ_{nm} is the Kronecker delta. The total field at $\vec{r}$, when all antennas are fed, is Bardati et al. [37]

$$\vec{E}(\vec{r}) = \sum_{m=1}^{M} \dot{V}_m \vec{e}_m(\vec{r}) \tag{8}$$

Using vector notations, the power absorbed by the target, averaged over a time period $T = f^{-1}$, is written as the following quadratic form:

$$P_\omega = P_0 \left[\dot{V}\right]^{T*} [Q] \left[\dot{V}\right] \tag{9}$$

where the dimensionless matrix $[Q]$ has elements

$$Q_{mn} = \frac{\sigma_e}{2P_0} \int_\omega \vec{e}_m^* \cdot \vec{e}_n \mathrm{d}V \tag{10}$$

and $\sigma_e = \sigma + 2\pi f \epsilon''$. σ and ϵ'' are tumour electrical conductivity and permittivity imaginary part, respectively, and are assumed constant in ω. In order to explain the name 'interference' given to $[Q]$, we note that an on-diagonal entry, say Q_{mm}, is power dissipation in ω due to interaction of electric field $\vec{e}_m$ and current $\sigma_e \vec{e}_m$ from the same mth generator. Instead, any off-diagonal entry, say Q_{mn} (Q_{nm}) with $m \neq n$, originates from interaction of the field (current) from the mth generator with the current (field) due to the nth one. Any phased array effect, i.e. interference, is taken into account by these cross terms.

Later we shall use an equation for P_ω in terms of waves. Taking Equations (7) and (9) into account we get

$$P_\omega = [a]^{T*} \left[\tilde{Q}\right] [a] \tag{11}$$

The matrix $\left[\tilde{Q}\right] = [D]^{-1}[Q][D]^{-1}$ has entries

$$\tilde{Q}_{mn} = Q_{mn} \sqrt{H_{mm} H_{nn}} \tag{12}$$

In conclusion, the powers delivered to the body and target, P_Ω and P_ω respectively, have been introduced as equations (quadratic forms) in two primary matrices $[H]$ and $[Q]$, and secondary ones $[\bar{H}]$ and $\left[\tilde{Q}\right]$. The key point is that these matrices are Hermitian and positive-definite (HP-D). Some properties of HP-D matrices are beneficial in solving the extremum (minimum-maximum) problem [38] we deal with in this paper. Noticeably, i) the diagonal entries and the eigenvalues of an HP-D matrix are real and strictly positive (i.e. non-zero); ii) the smallest (largest) eigenvalue is smaller (larger) than the smallest (largest) diagonal entry [39].

Feed efficiency

A suitable definition for feed efficiency is the portion of the available power from the sources that is supplied to the body:

$$\eta_F = P_\Omega / P_G \tag{13}$$

After substitution of Equations (2) and (3),

$$\eta_F = [a]^{T*}[H][a] / \left([a]^{T*}[a]\right) \tag{14}$$

$[H]$ has M real positive eigenvalues μ_m, $m = 1, \ldots, M$. Denoting $\mu_{\min} > 0$ and $\mu_{\max}$ the smallest and largest eigenvalues, respectively, then

$$\mu_{\min} \leq \eta_F \leq \mu_{\max} \tag{15}$$

[39, p. 272]. Due to the above property (ii), $\mu_{\min} < 1$. Further properties are reported in Appendix 2.

The following example may clarify the relevance of η_F and its bounds. Let an array be formed by $M = 2$ parallel dipoles in distilled water which radiate in front of a layered skin–fat–muscle arrangement. The same dipole and phantom will be taken up again in the numerical analysis section. In Figure 2, the eigenvalues μ_1 and μ_2 are diagrammed versus the spacing, s, between the dipoles. The diagrams show oscillations and crossings with role interchange between

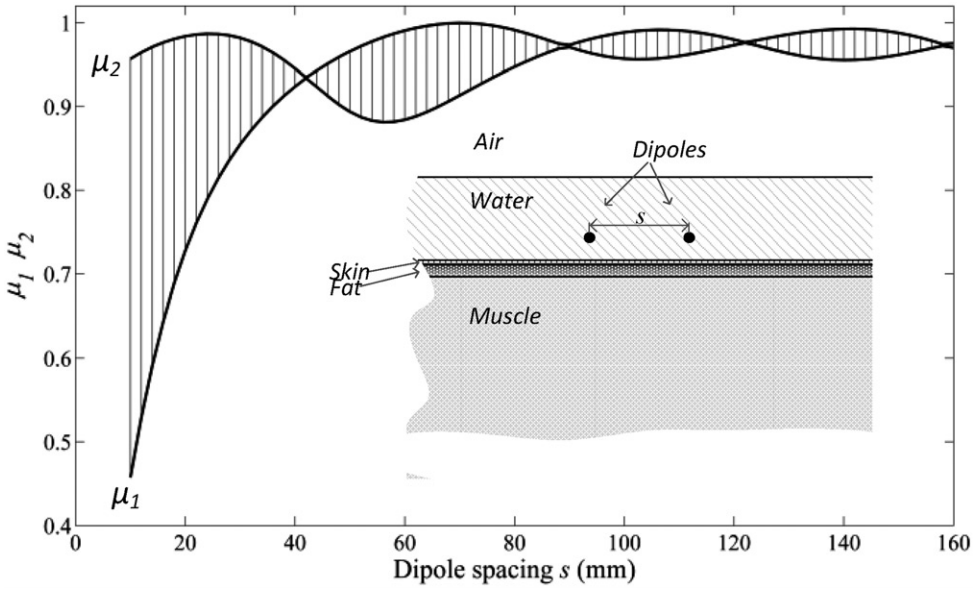

Figure 2. Eigenvalues μ_1 and μ_2 for a two-element array in front of a layered phantom (also shown in the inset) versus dipole spacing s. Depending on input setting $[a]$, feed efficiency η_F takes values in the dashed area between the μ_1, μ_2 curves.

larger and smaller eigenvalues. For any given spacing s, η_F lies in the range between the μ_1, μ_2 curves, its current value depending on feed $[a]$. In case of very close dipoles, some inputs may cause a low feed efficiency, while η_F is less dependent on $[a]$ when the distance between them is greater.

The largest (smallest) feed efficiency is obtained when $[a]$ is an eigenvector $[h]$ of $[H]$ corresponding to $\mu_{\max}$ ($\mu_{\min}$). Values of the feed efficiency are useful in estimating RF power requirements.

Targeting efficiency

A targeting (or focusing) efficiency η_T is introduced for evaluating system ability to couple radiation to the target as the fraction of power supplied by the generators to the body that is dissipated by the target:

$$\eta_T = P_\omega / P_\Omega \tag{16}$$

From Equations (9) and (5) the targeting efficiency is the following ratio of quadratic HP-D forms

$$\eta_T = \left[\dot{V}\right]^{T*}[Q]\left[\dot{V}\right] / \left(\left[\dot{V}\right]^{T*}[\bar{H}]\left[\dot{V}\right]\right) \tag{17}$$

η_T depends on the complex factor $\left[\dot{V}\right]$. The corresponding minimum-maximum problem is considered in Appendix 3, where it is shown that η_T is upper bounded according to

$$\eta_T \le \lambda_{\max} < \frac{T_{\tilde{Q}}}{\mu_{\min}} < \frac{T_Q}{\mu_{\min}} \tag{18}$$

where $\lambda_{\max}$ is the largest eigenvalue of a suitably defined problem, and

$$T_{\tilde{Q}} = \tilde{Q}_{11} + \tilde{Q}_{22} + \cdots + \tilde{Q}_{MM} = Q_{11}H_{11} + Q_{22}H_{22} + \cdots + Q_{MM}H_{MM} \tag{19}$$

is the trace of $\left[\tilde{Q}\right]$ from Equation (12). T_Q is the trace of $[Q]$ and $\mu_{\min}$ is defined by Equation (15).

The targeting efficiency is optimal and equal to $\lambda_{\max}$ when $\left[\dot{V}\right]$, that optimises η_T, is an eigenvector $\left[\dot{V}_T\right]$ corresponding to $\lambda_{\max}$. Under this hypothesis, $P_\omega = \lambda_{\max} P_\Omega$ where, from Equations (5) and (6),

$$P_\Omega = P_0 \sum_{m,n=1}^{M} \frac{H_{mn}}{\sqrt{H_{mm}H_{nn}}} \dot{V}^*_{T,m} \dot{V}_{T,n} \tag{20}$$

Here $\dot{V}_{T,m}$ denotes the mth component of $\left[\dot{V}_T\right]$. To remove an arbitrary amplitude factor, $\left[\dot{V}_T\right]$ is normalised to have $P_\Omega = P_0$ from Equation (20). It is worth observing that any set of feed voltages (strengths and phases) different from the eigenvectors causes a decrease of η_T.

When only one generator, say ℓ, is fired, then from Equations (6) and (17) $\eta_T = Q_{\ell\ell}/\bar{H}_{\ell\ell} = Q_{\ell\ell}$. Therefore, the on-diagonal terms of the interference matrix give the targeting efficiency of each antenna when it radiates in the presence of the others which have been kept off.

Heating efficiency

A familiar figure of merit of hyperthermia systems is heating efficiency, η_H. A possible definition, that is consistent with the above equations, is the fraction of available power from the generators that is absorbed in the target, i.e. Equation (21):

$$\eta_H = P_\omega / P_G \tag{21}$$

From Equations (13) and (16), $\eta_H = \eta_F \eta_T$. However, a discussion of η_H directly based on Equation (21) has some interest and is given hereafter. The use of $[a]$ as independent parameter is advantageous. From Equations (2) and (11) we get Equation (22):

$$\eta_H = [a]^{T*}\left[\tilde{Q}\right][a] / \left([a]^{T*}[a]\right) \tag{22}$$

The extremum problem is formulated as above for the other efficiencies giving Equation (23):

$$\eta_H \le \nu_{\max} < T_{\tilde{Q}} \tag{23}$$

where $\nu_{\max}$ is the largest eigenvalue of $\left[\tilde{Q}\right]$ and $T_{\tilde{Q}}$ is given by Equation (19). If the only mth channel is fired, then $\eta_H = \tilde{Q}_{mm} = H_{mm}Q_{mm}$ from Equation (12). Therefore, $T_{\tilde{Q}}$ is sum of the individual heating efficiencies when the sum is made all over the channels.

The best heating efficiency is obtained when $[a] = [a_H]$, i.e. an eigenvector of $\left[\tilde{Q}\right]$ corresponding to $\nu_{\max}$. Under best heating conditions $\eta_H = \nu_{\max}$, while the available power from the generators is $P_G = [a_H]^{T*}[a_H]$ from Equation (2), and the power to the target is $P_\omega = \nu_{\max}[a_H]^{T*}[a_H]$ from Equation (21). To remove an arbitrary factor from $[a_H]$ the condition $P_G = P_0$ is applied to the last equation. Therefore, under best heating condition the power delivered to the target is $\nu_{\max}P_0$.

Efficiency upper bounds

How close η_H is to the upper bound $T_{\tilde{Q}}$ depends on $\nu_{\max}$, which, in turn, depends on the off-diagonal elements of $\left[\tilde{Q}\right]$. For example, if $\tilde{Q}_{mn} = 0$ for any m,n with $m \neq n$, then $\nu_{\max}$ is equal to the largest on-diagonal element of $\left[\tilde{Q}\right]$. If, instead, $\tilde{Q}_{mn} \neq 0$ and, moreover,

$$\tilde{Q}_{mn}\tilde{Q}_{nm} \to \tilde{Q}_{mm}\tilde{Q}_{nn} \tag{24}$$

for any m,n then $\nu_{\max}$ is close to the trace of $\left[\tilde{Q}\right]$, i.e. the upper bound, as shown in Appendix 4. In the above limit, $\rho_{mn} = \tilde{Q}_{mn}\tilde{Q}_{nm}/(\tilde{Q}_{mm}\tilde{Q}_{nn})$ is almost unitary for any m,n and the sum of ρ_{mn} over the off-diagonal entries is equal to the number $M(M-1)$ of these entries. In the numerical analysis a filling index $\varepsilon < 1$

$$\varepsilon = \frac{1}{M(M-1)} \sum_{\substack{m,n=1 \\ m \neq n}}^{M} \frac{\tilde{Q}_{mn}\tilde{Q}_{nm}}{\tilde{Q}_{mm}\tilde{Q}_{nn}} \tag{25}$$

will be evaluated to estimate how close to Equation (24) an array is performing. In other words, since any power to the target due to source interference is taken into account by the off-diagonal entries of $\left[\tilde{Q}\right]$, a weighted average over these terms may be a suitable measure of the array effect. Similar considerations apply to $[Q]$.

The above considerations apply to a hyperthermia applicator where the electromagnetic field from the sources is entirely transmitted to the body under treatment and internal resistance of the sources, avoiding radiation to the environment. When stray radiation is non-negligible, a term P_{env} is included in the power balance to account for it. Moreover, some power P_{abs} is directly absorbed by the device, due to imperfectly conducting metals and imperfectly insulating dielectrics. Therefore, less power $P'_\Omega = P_\Omega - P_{env} - P_{abs}$ is transferred to the body under treatment [40]. It is worth noticing that Equation (21) for heating efficiency is independent of these loss terms which have, however, a separate important meaning. In fact, the safety of the patient and attendants from stray fields must be assured. In addition, the net power absorbed by the patient is evaluated for possible systemic stress. Finally, power dissipation in feed lines and device may cause undesired heating of the equipment.

Array factor

The overall benefit of a phased array may be estimated by an array factor that is the ratio of heating efficiencies as

$$G_H = \eta_H/\eta_H^\dagger \tag{26}$$

where η_H and $\eta_H^\dagger$ are evaluated by Equation (22) for amplitudes $[a_H]$ and $\left[a_H^\dagger\right]$, respectively, the latter still to specify. The best performing radiator (BPR) is characterised by the largest $\tilde{Q}_{mm}$, for $1 \leq m \leq M$. After renumbering, the BPR is marked 1. Then $\left[a^\dagger\right] = [1, 0, \ldots, 0]^T$ and $\eta_H^\dagger = \tilde{Q}_{11}$. Taking Equation (23) into account, upper bounds to G_H are

$$G_H \leq \frac{\nu_{\max}}{\tilde{Q}_{11}} < \frac{T_{\tilde{Q}}}{\tilde{Q}_{11}} \leq M \tag{27}$$

To obtain Equation (27) the inequality $T_{\tilde{Q}} \leq M\tilde{Q}_{11}$ was used. The equality holds when all heating efficiencies $\tilde{Q}_{mm}$ are equal, as may be the case in an annular phased array with the target in the middle. Such a phased array will have G_H close to M. In the numerical analysis a relative array factor $g_H = G_H/M < 1$ will be evaluated to appreciate how much a phased array behaves closely to an ideal one.

When the channels have equal heating efficiency $\tilde{q}$, i.e. $\tilde{Q}_{mm} = \tilde{q}$ for any m, then $\eta_H^\dagger = \tilde{q}$ and $\eta_H = \tilde{q}G_H$ from Equation (26). Therefore, the array efficiency is the product of the array factor and the individual efficiency. This result is similar to power pattern multiplication, which holds in phased array modelling under simplifying assumptions, when they are used to create radiation lobes in the far field [41]. Another similarity will be carried out in the numerical analysis. However, phase effects are dominated by field damping within interposed tissues in hyperthermia arrays. Furthermore, hyperthermia array modelling needs full wave solutions of the electromagnetic field equations in a region including antennas, bolus and patient body, which account for reflections, radiation and coupling.

Numerical analysis and results

A numerical analysis was performed to investigate how the above-defined efficiencies work in a possible array. The cylindrical dipole was elected as an elementary antenna because its poor directive properties [41] put phased array advantages into greater evidence. We adopted a plane layered skin–fat structure backed by a half-space of muscle as numerical phantom (Figure 3). w_s and w_f are thicknesses of the skin and fat layers, respectively.

The dipoles lie on a plane parallel to the tissue layering at a distance w_b from the skin surface (water-bolus thickness). On the other side of the dipoles, a second water layer is thick w_c and is backed by a half-space of air. The air–water interface will partially confine dipole back radiation [42]. Circulating distilled water within these two layers is predicted for cooling both tissues and dipoles. More sophisticated phantoms are currently adopted for general studies and treatment planning. However, they require a relatively long computation time, whereas fast computations are preferable when the array

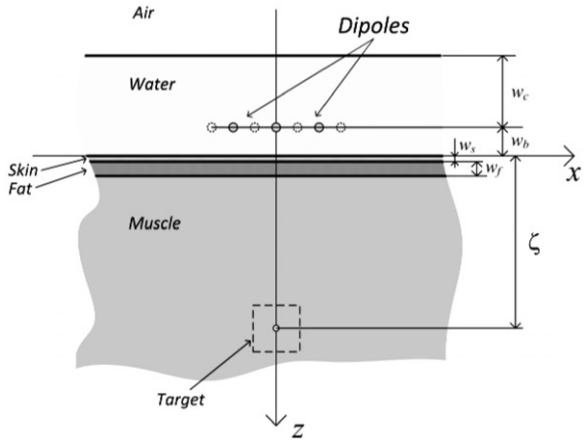

Figure 3. Planar multilayer phantom: $w_s = 4$ mm, $w_f = 10$ mm, $w_b = 20$ mm, $w_c = 50$ mm. A cube target with side 34.2 mm is also shown.

Table I. Physical parameters.

	ϵ_r	σ_e (Sm^{-1})
Muscle	57	0.80
Fat	5.6	0.04
Skin	46	0.70
Distilled water	80	0.04

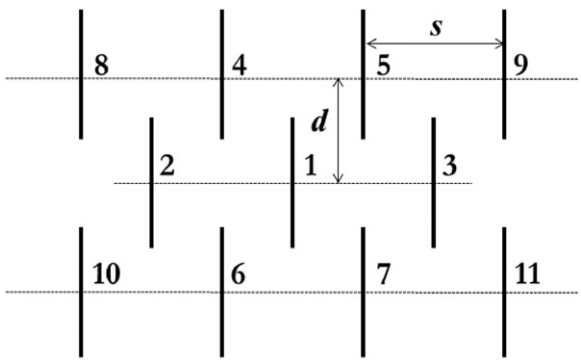

Figure 4. 11-element planar array. Row spacing d and dipole spacing s are free parameters in the numerical analysis.

response is investigated for small increments of the geometrical parameters. The tissue parameters (dielectric constant ϵ_r and effective conductivity σ_e) have been taken from IFAC-CNR [26] (Table I).

The coordinate system for this phantom has the z-axis perpendicular to the layering with the origin O at the skin–bolus interface. Centre-fed dipoles are directed along the y-axis, and their diameter (1.4 mm) and length ($l = 62$ mm) allow good matching to 50Ω cables for the array arrangements here analysed. Matching devices find application in practical systems, but they have less importance in this paper.

The basic 11-element array is shown in Figure 4. The dipoles have centres on equidistant parallel rows whose separation is the row distance, d. A partially interdigitated array is obtained for $d < l$. The spacing s between the next dipoles in the same row is constant for a given array. The dipoles in adjacent rows are shifted by $s/2$. The array effective area is here defined as the area A of the rectangle which strictly includes the dipoles preserving a margin $s/2$ and $d/2$ along $\pm x$ and $\pm y$, respectively. The target is modelled as a cube of volume $\tau = 40\,\text{cm}^3$ immersed in the muscle half space. For the sake of simplicity, its electrical parameters do not differ from those of the host tissue. The cube has sides of 34.2 mm, that are parallel to the coordinate axes. Its centre O_τ is distant ζ from the origin, i.e. $\overline{OO_\tau} = \zeta$. Spacing s, row distance d and target depth ζ are free parameters in the numerical simulation.

The proposed phantom allows the electromagnetic field problem to be solved by means of the Green function for planar multilayer media, allowing beneficial speed-up in computer time. Computations have been performed by means of a commercial solver, FEKO™ (EM Software & Systems, Stellenbosch, South Africa). MATLAB™ (Natick, MA, USA) has been used for algebraic operations on the field data provided by the solver.

According to Equation (15) $\mu_{\min}$ and $\mu_{\max}$ are lower and upper bound, respectively, of an interval of possible values for η_F. However, the lower bound may have more interest in applications than the upper one. Indeed, the power fraction from sources that is delivered to a body under treatment will never be less than $\mu_{\min}$, whatever complex factor $[\dot{V}]$ may result from treatment planning and optimisation. From this point of view, $\mu_{\min}$ should be as large as possible. Equivalently, the norm $\|S\|_2$ should be as small as possible.

The 11-element array's $\mu_{\min}$ is diagrammed in Figure 5. Starting from very close dipoles and increasing their distance, $\mu_{\min}$ increases to acceptable values, e.g. the power delivered to the body is $>0.65\ P_G$ in the range $35\,\text{mm} < s < 55\,\text{mm}$, $d > 50$ mm, where P_G, given by Equation (2) is the total available power from the generators. $\mu_{\max}$ has similar behaviour, but it remains >0.97 for any s, d in these ranges. Eigenvalues have been investigated up to s and d values which correspond to acceptable sizes for the entire array.

In Figure 6 $\lambda_{\max}$ and $\nu_{\max}$ are reported, which are upper bounds to η_T and η_H, respectively. The diagrams refer to the cube target at $\zeta = 60$ mm from the skin surface. Due to strong RF field damping with depth in tissue, $\lambda_{\max}$ and $\nu_{\max}$ take low values and, consequently, both efficiencies are quite low. The contour level plots exhibit a positive slope for small values of s, d and reach a flat top showing that row distance is less critical than dipole spacing.

A decrease of η_T and η_H for large s, d is due to a decrease in peripheral dipole heating efficiency when their distance to the target is increased. However, a suitable choice of the geometrical parameters in the above s, d ranges may double (triple) the η_T (η_H) upper bound. Both $\lambda_{\max}$ and $\nu_{\max}$ attain a flat top in a neighbourhood of $s_0 = 50$ mm, $d_0 = 52$ mm, which for brevity we will refer to as the optimal array sizes. Note that $s_0 = 0.65\lambda_w$ and $d_0 = 0.67\lambda_w$, where λ_w is the wavelength at 434 MHz in water. Similar quotients are common in classical array theory. If the efficiencies are calculated in s_0, d_0 for $[\dot{V}] = [\dot{V}_T]$, their values are $\eta_F = 0.763$, $\eta_T = 0.0173$, and $\eta_H = 0.0132$. If they are calculated for $[\dot{V}] = [\dot{V}_H]$, instead, $\eta_F = 0.783$, $\eta_T = 0.0171$, and $\eta_H = 0.0133$. From a practical point of view, delivering $P_0 = 1$ W to the target requires no less than $\eta_H^{-1} P_0 = 75.2$ W from the generators.

η_T and η_H have been calculated for continuous variation of target depth and $s = s_0$, $d = d_0$. The diagrams are almost linear on a logarithmic axis with slope -0.20 dB/mm.

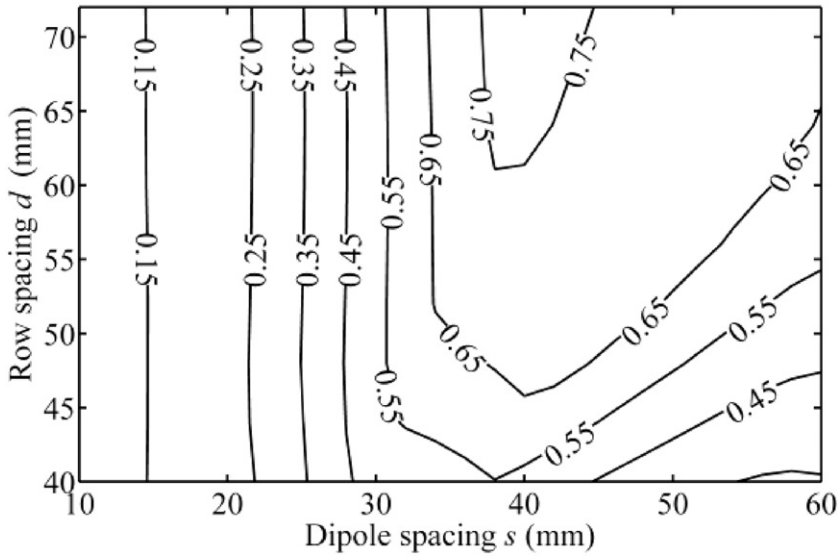

Figure 5. Smallest eigenvalue, $\mu_{\min}$, of matrix $[H]$ versus s and d.

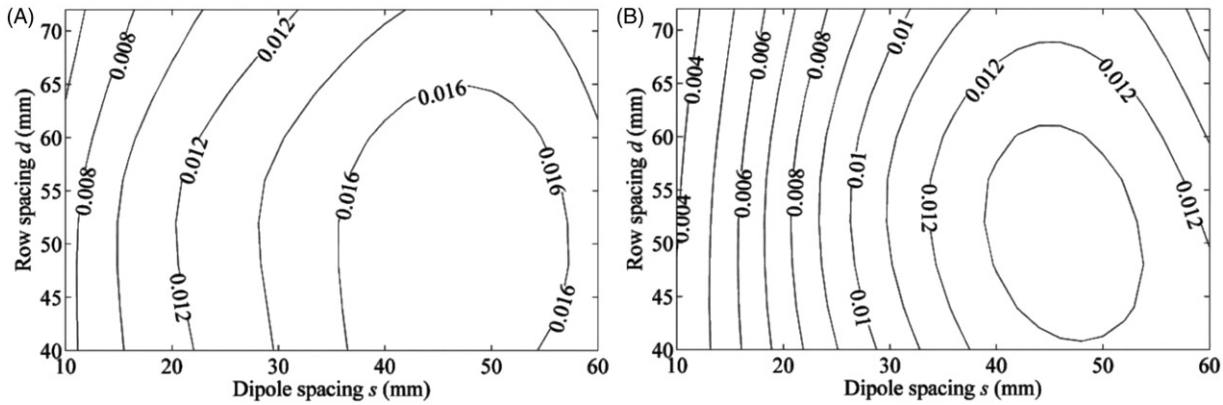

Figure 6. (A) $\lambda_{\max}$, and (B) $\nu_{\max}$ versus s and d.

The power requirement doubles when the target depth increases by about 15 mm. For comparison, the slope of a 434 MHz plane wave propagating in muscle is −0.16 dB/mm.

In Figure 7 the relative array factor g_H is plotted versus s and d, for $\zeta = 60$ mm. We reformulate g_H as product of two factors

$$g_H = \frac{T_{\tilde{Q}}}{\tilde{Q}_{11} M} \frac{\nu_{max}}{T_{\tilde{Q}}} \tag{28}$$

The first factor is 1 if the heating efficiencies $\tilde{Q}_{mm}$ are equal for all radiators, while $\nu_{\max}/T_{\tilde{Q}} \to 1$ if the condition in Equation (24) applies. For $s = s_0$, $d = d_0$ the relative array factor is $g_H \cong 0.28$, while the two factors are 0.33 and 0.84, respectively. Therefore, the relatively low value of g_H is due more to the poor heating efficiency of the peripheral dipoles 8, 9, 10, and 11 than to weak coupling among them and the best performing dipole.

From Equation (25), the filling index ε is 0.74. ε decreases slowly when s and d increase, varying less than ±10% in the explored region. Indeed, the decrease of $\tilde{Q}_{mn}\tilde{Q}_{nm}$ with the distance between dipoles is smoothed out by the decrease of the terms $\tilde{Q}_{mm}$ and $\tilde{Q}_{nn}$ in the ratio.

When the target depth is varied, the moduli $\left|\dot{V}_{Tm}\right|$, that optimise η_T, exhibit small dependence on ζ, e.g. the change in $\left|\dot{V}_{T1}\right|$ is <12% for $35 < \zeta < 80$ mm. For optimal array sizes, the optimal complex factors are $\dot{V}_{T1} = 0.571\angle 0°$, $\dot{V}_{T2} = \dot{V}_{T3} = 0.368\angle 29.4°$, $\dot{V}_{T4} = \dot{V}_{T5} = \dot{V}_{T6} = \dot{V}_{T7} = 0.302\angle 41.4°$, $\dot{V}_{T8} = \dot{V}_{T9} = \dot{V}_{T10} = \dot{V}_{T11} = 0.173\angle 114.0°$. In case of η_H optimisation, similar results are obtained, which are not given here for brevity. The largest difference $\left|\dot{V}_{Tm}\right| - \left|\dot{V}_{Hm}\right|$ for $m = 1, \ldots, M$, is 0.018 when both eigenvectors are normalised according to $P_{\Omega} = 1$ W.

Let $P_d(\vec{r}) = 1/2\sigma_e \left|\vec{E}(\vec{r})\right|^2$ be power loss density at point $\vec{r}$, where $\vec{E}$ is obtained by Equation (8) for $\left[\dot{V}\right] = \left[\dot{V}_T\right]$, after η_T (or η_H) optimisation. We denote $P_{d,\max}$ the maximum of $P_d(\vec{r})$ when $\vec{r}$ spans the bolus–skin interface. In our example $P_{d,\max} = 6.7\ \text{mW cm}^{-3}$ for $P_{\Omega} = 1$ W to the body. The following considerations are intended to provide insight into an acceptable value for $P_{d,\max}$.

When the problem of skin protection from hot spots is considered, radiation of the whole P_{Ω} by a single dipole is the worst case. For the sake of simplicity we model the dipole's field entering the body as a patch of plane wave having the area sd. The power density carried by the wave is $P = P_{\Omega}/(sd)$. A familiar equation gives $P_{d0} = 2\alpha P$ for

Figure 7. Relative array factor g_H as a function of s and d.

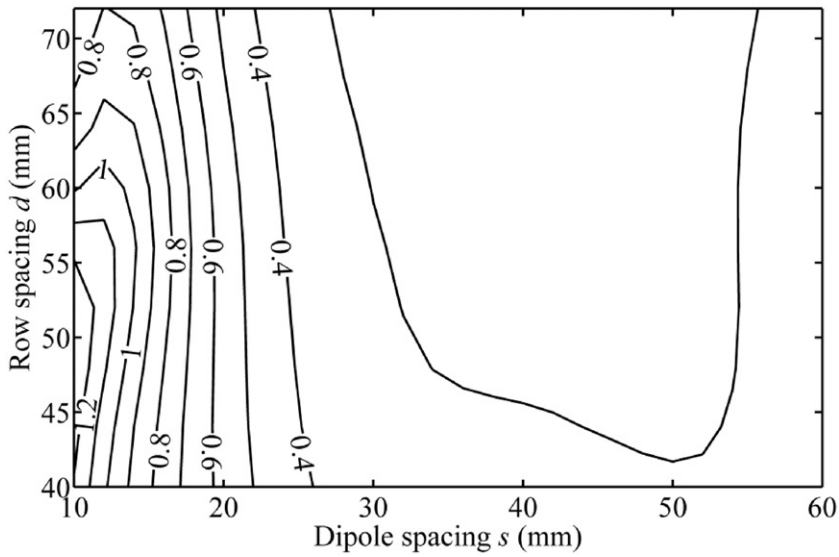

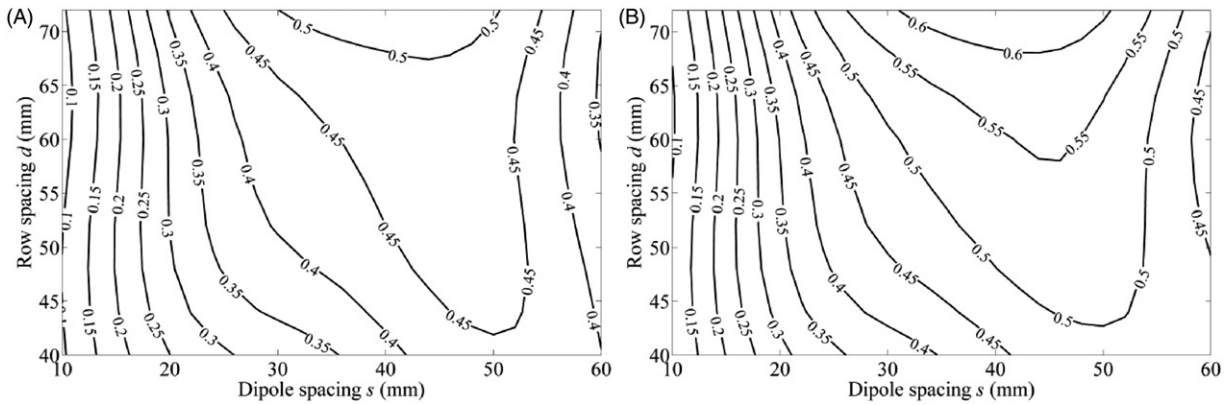

Figure 8. β_T versus s and d, (A) for $\zeta = 60$ mm, (B) for $\zeta = 40$ mm. $\alpha = 0.0186\,\text{mm}^{-1}$.

power dissipation by a plane wave, where the damping coefficient α is the reciprocal of the penetration depth in the skin [26]. P_{d0} is taken as a reference value for $P_{d,\,\max}$, so that a new parameter β_T is introduced as

$$\beta_T = \frac{P_{d,\max}}{P_{d0}} = \frac{sdP_{d,\max}}{2\alpha P_\Omega} \tag{29}$$

For skin protection from hot spots β_T should be small. According to this parameter the array with the lowest $sdP_{d,\,\max}$ will be preferred. In Figure 8, β_T is plotted vs.s and d, for two target depths.

The β_T diagrams show minor dependence on row spacing, and an almost flat top for dipole spacing in the range between 30 and 50 mm. The maximum power loss on the skin surface decreases approximately inversely with d and for s in the above range. For $s = s_0$, $d = d_0$ we get $\beta_T = 0.47$ for $\zeta = 60$ mm and $\beta_T = 0.53$ for $\zeta = 40$ mm. The model for β_T does not take into account the real electromagnetic field distribution in the body, which, however, is generally unavailable when the array is developed.

A further figure of merit is the ratio of the largest amplitude to the smallest one in the open circuit voltages, following an η_H optimisation. Taking Equation (7) into account,

$$\gamma_H = \frac{\max\limits_{m=1,\,\ldots,\,M} |a_{H,\,m}|}{\min\limits_{m=1,\,\ldots,\,M} |a_{H,\,m}|} \tag{30}$$

Measuring an imbalance in the feed system, the parameter $\gamma_H \geq 1$ is often evaluated for array characterisation in other branches of engineering. A lower value of γ_H is preferable since it corresponds to a better use of the available power of the sources. This is easily verified in the case of $M = 2$ radiators. Let $P_{av,\,\max}$ be the maximum power that is available from each source, while $P_{\omega,\,\max}$ is the power that the array can deliver to the target ω under optimal heating efficiency operation. From Equations (21) and (30),

$$P_{\omega,\,\max} = \eta_H P_{av,\,\max}\left(1 + 1/|\gamma_H|^2\right) \leq M\eta_H P_{av,\,\max} \tag{31}$$

where the equality holds when $\gamma_H = 1$.

For $s = s_0$, $d = d_0$, the components of $[V_{oc}] = \sqrt{8R_0}[a_H]$ following heating efficiency optimisation and eigenvector normalisation, are $V_{oc1} = 11.44\angle 0°$, $V_{oc2} = V_{oc3} = 6.92\angle 38.4°$, $V_{oc4} = V_{oc5} = V_{oc6} = V_{oc7} = 5.76\angle 37.8°$, $V_{oc8} = V_{oc9} =$

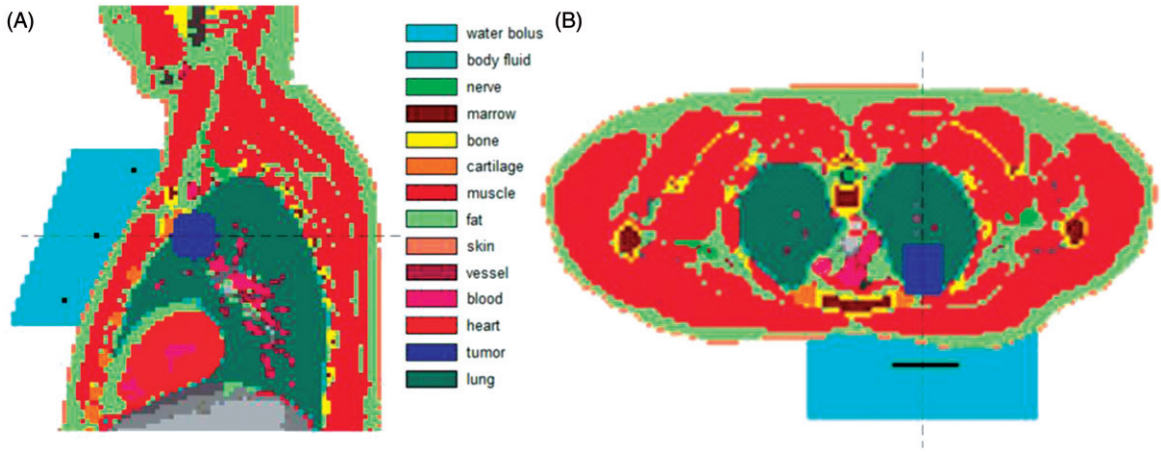

Figure 9. (A) Sagittal and (B) transverse images from the Visible Human Project (male). A cylindrical tumour and a water bolus containing the dipoles are included.

$V_{oc10} = V_{oc11} = 3.20\angle 128.4^\circ$ (voltages in V). $\gamma_H = 3.58$ is obtained. The corresponding available powers are obtained as $P_{av,1} = 0.326$, $P_{av,2} = P_{av,3} = 0.119$, $P_{av,4} = P_{av,5} = P_{av,6} = P_{av,7} = 0.083$, and $P_{av,8} = P_{av,9} = P_{av,10} = P_{av,11} = 0.026$, for 1 W of total available power P_G from the generators. Taking Equation (21) into account, the available powers for 1 W to the target are directly obtained by multiplying these $P_{av,m}$ by $\eta_H^{-1} = 75.2$, e.g. the generator feeding the BPR will provide 24.5 W. It is worth observing that the above analysis provides a top value $P_{\omega,\,\max}$, i.e. a simple equation between ratios gives $P_{\omega,\,\max} = P_{av,\,\max}/24.5$.

Together the peripheral radiators deliver about 10% of the total power and could represent clinically irrelevant settings [25]. Therefore, a 7-element array was investigated after removing the peripheral dipoles. The steps of the previous analysis were repeated and the numerical results for $\zeta = 60$ mm target depth are reported hereafter for comparison. The array parameters, which optimise η_T, are found as $s = 58$ mm, $d = 48$ mm, for a less effective area A (-14.3%). Following an η_T (η_H) optimisation, the efficiencies are obtained as $\eta_F = 0.802$ (0.818), $\eta_T = 0.0141$ (0.0140), and $\eta_H = 0.0113$ (0.0114). An 18.5% reduction in η_T as well as a 14.4% reduction in η_H can be appreciated. The relative array factor, factorised as in Equation (28), is $g_H = 0.57 * 0.90 = 0.51$ with improvement in comparison with the 11-element array. Accordingly, the filling index of the interference matrix is evaluated as $\varepsilon = 0.87$, versus 0.74 of the 11-element array. The parameter β_T takes a lightly lower value (0.44) showing a more uniform power loss distribution on the bolus/skin interface. The open-circuit voltage amplitudes (in V) of the generator set, normalised to have $P_G = P_0$, are obtained as $V_{oc1} = 10.6\angle 0^\circ$, $V_{oc2} = V_{oc3} = 7.19\angle 52.1^\circ$, $V_{oc4} = V_{oc5} = V_{oc6} = V_{oc7} = 6.81\angle 27.6^\circ$. $\gamma_H = 1.56$ is obtained. The corresponding available powers are $P_{av,1} = 0.279$, $P_{av,2} = P_{av,3} = 0.129$, and $P_{av,4} = P_{av,5} = P_{av,6} = P_{av,7} = 0.116$ (in W). They are scaled to 24.4, 11.3, and 10.2 W in that order, for 1 W to the target. The best performing dipole's available power is practically the same for both arrays. In conclusion, the 7-element array needs more power than the 11-element one for the same power delivered to the target, but the power demand is better balanced in the radiators.

The proposed means and methods were further checked by a numerical analysis performed for a heterogeneous and complex anatomical structure. Anthropomorphic data from the Visible Human Project (male) (VHP) were used [43]. To reduce the computational costs, the data set for the upper trunk was re-sampled as a $4 \times 4 \times 4\,\text{mm}^3$ grid. Cartesian axes were introduced so that the coordinate planes were the body planes of the VHP images. Each body and tissue boundary was approximated by staircasing, each cell having sides parallel to the axes. The technique used for re-sampling is referred to as the winner-takes-all technique: a low resolution cell is assigned the dielectric properties of the tissue type that fills the largest fraction of its volume [44]. A cylindrical tumour of about $40\,\text{cm}^3$ was positioned within the left lung close to the visceral pleura. The tumour's centre distance from the skin is 6 cm. The tumour's diameter and length are 20 mm and 32 mm, respectively. Sagittal and transverse images through the tumour's centre are shown in Figure 9. The healthy tissue parameters have been taken from IFAC-CNR [26]. Separate computations were performed for a deflated and inflated lung.

The values for the tumour were taken from Joines et al. [45] as 55.5 for relative permittivity and 0.94 S/m for conductivity. The 7-element array with s and d already optimised for the layered phantom was positioned at an average distance of 2 cm from the trunk. To keep the dipoles at a uniform distance from the chest avoiding staircasing of the dipoles, they were drawn horizontally (i.e. parallel to the transversal planes) on an oblique plane. A privileged position was reserved for dipole 1 in front of the tumour. A $20 \times 15 \times 7\,\text{cm}^3$ box of distilled water (bolus) was also positioned in front of the body, as shown in Figure 9, with the dipoles inside. Water and skin are in contact. The overall computation domain is a box of 198×130 cells in the transversal plane and 210 cells in the axial (vertical) direction. The portion of the box that is not filled with body, dipoles or bolus is air. BEST, a proprietary FDTD code [46], was used for electromagnetic field calculation, and then matrix and eigenvalue computations were performed by the same codes already used for the layered phantom. BEST uses an iterative algorithm which stops when a well-defined overall error is less than 0.01. The computer time for one set of the array's

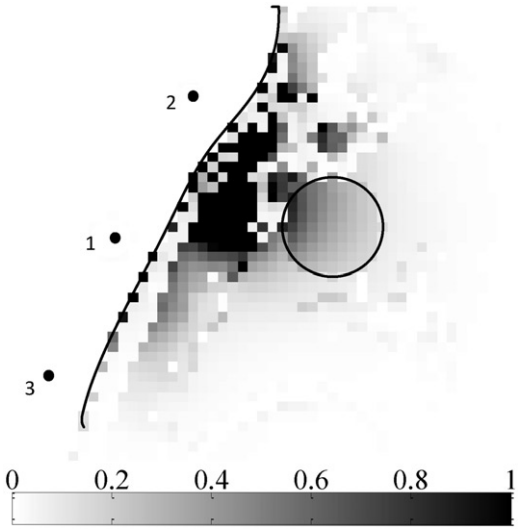

Figure 10. Power deposition (mW/cm^3) in the sagittal plane through the tumour centre, for $P_\Omega = 1$ W. Skin–bolus interface and tumour border are marked by solid lines. $P_{d,max} = 10$ mW/cm^3. Dipoles 1–3 are also shown.

parameters and one source was 5 h for the anthropomorphic phantom. For comparison, the corresponding time for the layered phantom was 15 s with the FEKO solver. It is worth observing that the two codes follow two different schemes: BEST is an FDTD solver, while FEKO is based on a method of moment algorithm [47].

Initially, the results for the deflated lung were compared with those for the inflated one. Relevant changes in matrices $[S]$, $[H]$ and $[Q]$ were not appreciated. Indeed, the largest deviation in the scattering matrix entries was 0.006 (for comparison, $|S_{11}| = 0.227$ for the inflated lung). The largest deviations in $|H_{mn}|$ and $|Q_{mn}|$ were less than 0.004 and 0.0008, respectively, where, for comparison, $H_{11} = 0.782$ and $Q_{11} = 0.0086$ for the inflated lung. Having more lung in its field of view in comparison with the other dipoles, dipole 3 was mainly responsible for these small changes passing from deflated to inflated.

Passing from the layered phantom to the anthropomorphic ones modifies the system matrices to an appreciable amount. Smaller changes in $[H]$ are observed (<11%). Indeed, the dipoles are immersed in distilled water in all models, while matching and direct coupling (which determine $[H]$) strongly depend on the dielectric properties of the medium in close proximity of dipoles. Instead, the larger changes in $[Q]$ (up to 55%) are due to the different dielectric characteristics of the tissues where propagation takes place. In addition, the role of the best performing radiator is partially shared by dipole 1 with dipole 2. Nonetheless, the largest eigenvalue of $[Q]$ does not differ significantly being 0.013 and 0.016 for the layered and anthropomorphic phantoms, respectively. The best targeting efficiency is 0.016 for the anthropomorphic phantom and 0.014 for the layered one. The best heating efficiency is 0.013 and 0.011 in the two cases, respectively.

A plot of power dissipation is shown in Figure 10 for the inflated lung phantom. Due to large values of power loss in the skin we get $\beta_T = 0.91$. The same parameters, s and d, that solved the optimisation problem for the layered structure have been used. Their optimisation for the anthropomorphic phantom is beyond the scope of this paper. The performed analysis, however, shows that the given definitions of efficiencies and bounds may be exploited for realistic structures.

The above numerical analysis has been restricted to planar arrays, for which the requirement of low direct coupling for high η_F partially conflicts with that of strong coupling of radiated fields in the target for high η_T. These requirements instead may not conflict in an annular phased array with the target in the middle of the ring, since the physical separation between adjacent antennas can be large enough for low direct coupling and potentially high feed efficiency, while opposite antennas may contribute comparable fields to the target, enabling constructive interference. However, when the target is not located in the middle, as may be the case for the tumour we deal with in the example, the possibility of aggression by means of a planar array from the closest external surface has been explored.

Conclusion

We summarise the conditions for optimal power delivery to a target by a phased array of M radiators: (i) $\tilde{Q}_{11}M$ should be as large as possible, where $\tilde{Q}_{11}$ is best performing radiator efficiency; (ii) the targeting efficiency of all radiators should be comparable with that of the best performing one; (iii) the entries of the scattering matrix $[S]$ should be as small as possible; and (iv) the largest eigenvalue of the interference matrix should be close to the bound, that is obtained if the off-diagonal terms are geometrical mean of the corresponding on-diagonal terms for large filling index ε. Some conditions may conflict in array design. Efficiencies and other figures of merit can be combined to formulate an objective function when global optimisation techniques are exploited. Global optimisation, not considered in this paper, will be investigated subsequently.

Acknowledgement

The authors wish to thank Gaetano Marrocco for assistance with BEST.

Declaration of interest

The authors report no conflicts of interest. The authors alone are responsible for the content and writing of the paper.

References

1. Overgaard J, Gonzalez Gonzalez D, Hulshof MC, Arcangeli G, Dahl O, Mella O, et al. Randomized trial of hyperthermia as adjuvant to radiotherapy for recurrent or metastatic malignant melanoma. Lancet 1995;345:540–3.
2. Vernon CC, Hand JW, Field SB, Machin D, Whaley JB, van der Zee J, et al. Radiotherapy with or without hyperthermia in the treatment of superficial localized breast cancer: Results from five randomized controlled trials. International Collaborative Hyperthermia Group. Int J Radiat Oncol Biol Phys 1996;35:731–44.
3. Sneed PK, Stauffer PR, McDermott MW, Diederich CJ, Lamborn KR, Prados MD, et al. Survival benefit of hyperthermia in a prospective randomized trial of brachytherapy boost ± hyperthermia for glioblastoma multiforme. Int J Radiat Oncol Biol Phys 1998;40:287–95.
4. Van der Zee J, Gonzalez Gonzalez D, van Rhoon GC, van Dijk JD, van Putten WL, Hart AA, for the Dutch Deep Hyperthermia Group. Comparison of radiotherapy alone with radiotherapy plus

hyperthermia in locally advanced pelvic tumors: A prospective, randomised, multicentre trial. Lancet 2000;355:1119–25.
5. Rau B, Wust P, Hohenberger P, Loeffel J, Huenerbein M, Below C, et al. Preoperative hyperthermia combined with radio chemotherapy for locally advanced or recurrent rectal cancer: A phase II clinical trial. Annals of Surgery 1998;227:380–9.
6. Van de Kamer JB, de Loew AA, Hornsleth SN, Kroeze H, Kotte AN, Lagendijk JJ. Development of a regional hyperthermia treatment planning system. Int J Hyperthermia 2001;17: 207–20.
7. Kok HP, Van Haaren PM, Van de Kamer JB, Wiersma J, van Dijk JD, Crezee J. High resolution temperature-based optimization for hyperthermia treatment planning. Phys Med Biol 2005;50:3127–41.
8. Turner PF. Regional hyperthermia with an annular phased array. IEEE Trans Biomed Eng 1984;31:106–14.
9. Sapozink MD, Gibbs FA, Gibbs P, Stewart JR. Phase I evaluation of hyperthermia equipment – University of Utah Institutional Report. Int J Hyperthermia 1988;4:117–32.
10. Turner PF, Schaefermeyer T. BSD-2000 approach for deep local and regional hyperthermia: Clinical utility. Strahlenther Onkol 1989;165:700–704.
11. van Dijk JDP, Schneider C, van Os R, Blank LE, Gonzalez DG. Results of deep body hyperthermia with large waveguide radiators. Adv Exp Med Biol 1990;267:315–19.
12. Crezee J, Kok HP, Wiersma J, van Stam G, Sijbrands J, Bel A, et al. Improving locoregional hyperthermia equipment using 3-D power control: From AMC-4 to AMC-8. Proc 22nd Annu Meeting ESHO, Graz, Austria, 8-11 June 2005;14–15.
13. Nadobny J, Wlodarczyk W, Westhoff L, Gellermann J. Development and evaluation of a three-dimensional hyperthermia applicator with water-coated antennas (WACOA). Med Phys 2003; 30:2052–64.
14. Paulides MM, Bakker JF, Neufeld E, van der Zee J, Jansen PP, Levendag PC, et al. The HYPERcollar: A novel applicator for hyperthermia in the head and neck. Int J Hyperthermia 2007;23: 567–76.
15. Seebass M, Beck R, Gellermann J, Nadobny J, Wurst P. Electromagnetic phased arrays for regional hyperthermia: Optimal frequency and antenna arrangement. Int J Hyperthermia 2001;17:321–36.
16. Wust P, Seebass M, Nadobny J, Deuflhard P, Moenich G, Felix R. Simulation studies promote technological development of radiofrequency phased array hyperthermia. Int J Hyperthermia 2009;25: 517–28.
17. Canters RAM, Wust P, Bakker JF, Van Rhoon GC. A literature survey on indicators for characterisation and optimisation of SAR distributions in deep hyperthermia, a plea for standardization. Int J Hyperthermia 2009;25:593–608.
18. Franckena M, Canters R, Termorshuizen F, Van der Zee J, Van Rhoon G. Clinical implementation of hyperthermia treatment planning guided steering: A cross over trial to assess its current contribution to treatment quality. Int J Hyperthermia 2010;26: 145–57.
19. Magin RL, Peterson AF. Non-invasive microwave phased arrays for local hyperthermia: A review. Int J Hyperthermia 1989;5:429–50.
20. Paulsen KD, Geimar S, Tang J, Boyse WE. Optimization of pelvic heating rate distributions with electromagnetic phased arrays. Int J Hyperthermia 1999;15:157–86.
21. Kroeze H, van de Kamer JB, De Leeuw AAC, Lagendijk JJW. Regional hyperthermia applicator design using FDTD modeling. Phys Med Biol 2001;46:1919–35.
22. Paulides MM, Bakker JF, Zwamborn AP, Van Rhoon GC. A head and neck hyperthermia applicator: Theoretical antenna array design. Int J Hyperthermia 2007;23(1):59–67.
23. Fatehi D, Van der Zee J, Van Rhoon GC. Intra-patient comparison between two annular phased array applicators, Sigma-60 and Sigma-Eye: Applied RF powers and intraluminally measured temperatures. Int J Hyperthermia 2011;27:214–23.
24. De Greef M, Kok HP, Bel A, Crezee J. 3D versus 2D steering in patient anatomies: A comparison using hyperthermia treatment planning. Int J Hyperthermia 2011;27:74–85.
25. Kok HP, De Greef M, Borsboom PP, Bel A, Crezee J. Improved power steering with double and triple ring waveguide systems: The impact of the operating frequency. Int J Hyperthermia 2011;27: 224–39.
26. IFAC-CNR Institute for Applied Physics Nello Carrara. Available from http://niremf.ifac.cnr.it/tissprop/htmlclie/htmlclie.htm.
27. Bakker JF, Paulides MM, Westra AH, Schippers H, van Rhoon GC. Design and test of a 434 MHz multi-channel amplifier system for targeted hyperthermia applicators. Int J Hyperthermia 2010;26: 158–70.
28. Nadobny J, Fahling H, Hagmann MJ, Turner PF, Wlodarczyk W, Gellermann JM, et al. Experimental and numerical investigation of feed-point parameters in a 3-D hyperthermia applicator using different FDTD models of feed networks. IEEE Trans Biomed Eng 2002;49:1348–59.
29. Leybovich LB, Myerson RJ, Emami B, Straube WL. Evaluation of the Sigma 60 applicator for regional hyperthermia in terms of scattering parameters. Int J Hyperthermia 1991;7:917–35.
30. Lorrain P, Corson DR, Lorrain F. Electromagnetic Fields and Waves. New York: Freeman, 1988.
31. Duck FA. Physical Properties of Tissues. A Comprehensive Reference Book. London: Academic Press, 1990.
32. Raskmark P, Larsen T, Hornsleth SN. Multi-applicator hyperthermia system description using scattering parameters. Int J Hyperthermia 1994;10:143–51.
33. Pozar D. Microwave Engineering (3rd edn). New York: Wiley, 2005, p. 170.
34. Sadiku, MNO. Numerical Techniques in Electromagnetics. Boca Raton: CRC Press, 1995.
35. Taflove A. Advances in Computational Electrodynamics. The Finite-Difference Time Domain Method. Boston: Artech House, 1998.
36. Helzsajn J. Dissipation and scattering matrices of lossy junctions. IEEE Trans Microwave Theory Techn 1972;20:779–82.
37. Bardati F, Borrani A, Gerardino A, Lovisolo GA. SAR optimization in a phased array radiofrequency hyperthermia system. IEEE Trans Biomed Eng 1995;42:1201–07.
38. Abramowitz M, Stegun CA. Handbook of Mathematical Functions with Formulas, Graphs, and Mathematical Tables (9th edn). New York: Dover, 1972, 14.
39. Zhang F. Matrix Theory. Basic Results and Techniques (2nd edn). New York: Springer, 2011.
40. Van Rhoon GC, Rierveld PJM, Van der Zee J. A 433 MHz lucite cone waveguide applicator for superficial hyperthermia. Int J Hyperthermia 1998;14:13–27.
41. Balanis CA. Antenna Theory. Analysis and Design (3rd edn). New York: Wiley, 2005.
42. Sathiaseelan V, Iskander MF, Howard GCW, Bleehen NM. Theoretical analysis and clinical demonstration of the effect of power pattern control using the annular phased-array hyperthermia system. IEEE Trans Microwave Theory Techn 1986;34: 514–19.
43. Ackerman MJ. The Visible Human Project: A resource for education. Acad Med 1999;74:667–70.
44. Van de Kamer JB, De Leeuw AAC, Hornsleth SN, Kroeze H, Kotte ANTJ, and Lagendijk JJW. Development of a regional hyperthermia treatment planning system. Int J Hyperthermia 2001;17:207–20.
45. Joines WT, Zhang Y, Li C, Jirtle RL. The measured electrical properties of normal and malignant human tissues from 50 to 900 MHz. Med Phys 1994;21:547–50.
46. Marrocco G. RFID antennas for the UHF remote monitoring of human bodies. Paper presented at the IET Seminar on Antennas and Propagation for Body-Centric Wireless Communications, London, 24 April 2007, pp. 51–56.
47. Harrington RF. Field Computation by Moment Methods. New York: Macmillan, 1968.
48. Wilkinson JH. The Algebraic Eigenvalue Problem. London: Oxford University Press, 1965.
49. Van Trees HL. Optimum Array Processing. New York: Wiley, 2002, p. 449.

Appendix 1. P_Ω reformulation in terms of the complex factor

Taking Equations (1), (3) and (4) into account

$$P_\Omega = P_0 \left[\dot{V}\right]^{T*} [\bar{H}] \left[\dot{V}\right] = P_0 \sum_{m,n=1}^{M} \bar{H}_{mn} \dot{V}_m^* \dot{V}_n \tag{32}$$

where $P_0 = 1$ W is the reference power, $[\dot{V}]$ is the complex factor vector, and

$$\bar{H}_{mn} = (8R_0P_0)^{-1} H_{mn} u_m u_n \tag{33}$$

for any m, n. Nominal voltage u_m is chosen such that the power delivered to Ω through antenna m is P_0 when $V_{oc,m} = u_m$ and the remaining generators are switched off, i.e. $\dot{V}_n = \delta_{mn}$, $n = 1, \ldots, M$. From Equations (32) and (33) we obtain Equation (6) and

$$u_m = (8R_0P_0/H_{mm})^{1/2} \tag{34}$$

For compact matrix notation a real diagonal matrix $[D] = diag(H_{11}^{-1/2}, H_{22}^{-1/2}, \ldots, H_{MM}^{-1/2})$ is introduced so that

$$\bar{H} = [D][H][D] \tag{35}$$

From Equations (4), (34), and (35) we get $[V_{oc}] = \sqrt{8R_0P_0}[D]\left[\dot{V}\right]$ and, by comparison with Equation (1), we obtain Equation (7) in the main body.

Appendix 2. $[H]$ connection to the $[S]$ matrix

The extremal properties of the Rayleigh quotient in Equation (14) can be obtained through the eigenvalues of the Hermitian matrix $[S]^{T*}[S]$, which has real non-negative eigenvalues κ [48, p. 56]. If $\kappa_{\max}$ and $\kappa_{\min} \geq 0$ are the largest and smallest eigenvalues of $[S]^{T*}[S]$, respectively, then $\mu_{\min} = 1 - \kappa_{\max}$ and $\mu_{\max} = 1 - \kappa_{\min}$. Note that $\mu_{\max} \leq 1$. Interestingly, $\kappa_{\max} = (\|S\|_2)^2$, where $\|S\|_2$ is the spectral norm of $[S]$ [48, p. 57].

Appendix 3. Maxima and minima

As far as the extremisation of the ratio of Hermitian positive definite quadratic forms in C^M is concerned, we pose

$$\rho = \frac{\left[\dot{V}\right]^{T*} [Q] \left[\dot{V}\right]}{\left[\dot{V}\right]^{T*} [\bar{H}] \left[\dot{V}\right]} \tag{36}$$

for the real positive function ρ. The on-going formulation can be extended to the case where the matrix in the denominator is changed to $[I]$, to include the problems in Equations (14) and (22), with $[a]$ in place of $\left[\dot{V}\right]$. A vector $\left[\dot{V}\right]$ which extremises ρ, is an eigenvector [49] belonging to the eigenvalue λ of the following generalised Hermitian eigenvalue problem (GHEP)

$$[Q] \left[\dot{V}\right] = \lambda [\bar{H}] \left[\dot{V}\right] \tag{37}$$

Standard mathematical codes provide numerical solutions to the GHEP. The following considerations are performed to assess upper bounds to the efficiencies.

Since $[D]^{-1}[D] = [I]$, the numerator in Equation (36) is changed to $\left[\dot{V}\right]^{T*} [D][D]^{-1}[Q][D]^{-1}[D]\left[\dot{V}\right]$. Taking Equation (35) into account, we reformulate ρ as

$$\rho = \frac{\left[\ddot{V}\right]^{T*} \left[\tilde{Q}\right] \left[\ddot{V}\right]}{\left[\dot{V}\right]^{T*} [H] \left[\dot{V}\right]} \tag{38}$$

where $\left[\ddot{V}\right] = [D]\left[\dot{V}\right]$. Let $\lambda_{\max}$ ($\lambda_{\min}$) be the largest (smallest) eigenvalue of $\left[\tilde{Q}\right][H]^{-1}$. It is possible to show [39, p. 273] that

$$\lambda_{\min} \leq \rho \leq \lambda_{\max} \tag{39}$$

The last equation is true if $\left[\tilde{Q}\right]$ is Hermitian and $[H]$ is positive definite, as they are. We are interested in an upper bound to $\lambda_{\max}$. Using a result in Zhang [39, p. 274] the following inequality can be shown true:

$$\lambda_{\max} \leq \nu_{\max} \varphi_{\max} = \nu_{\max}/\mu_{\min} \tag{40}$$

where $\nu_{\max}$ and $\varphi_{\max}$ are the largest eigenvalues of $\left[\tilde{Q}\right]$ and $[H]^{-1}$, respectively, while $\mu_{\min} = 1/\varphi_{\max}$ is the smallest eigenvalue of $[H]$. Since the trace of a matrix is the sum of its eigenvalues while all the eigenvalues of a HP-D matrix are strictly positive, we get $\nu_{\max} < T_{\tilde{Q}}$ and $\lambda_{\max} < T_{\tilde{Q}}/\mu_{\min}$. Since all H_{mm} are <1, we get $T_{\tilde{Q}} < T_Q$ from Equation (19). Finally $\eta_T < T_Q/\mu_{\min}$.

Appendix 4. Getting closer to the theoretical upper bound

It is worth exploring under which circumstances $\nu_{\max}$ is close to the bound $T_{\tilde{Q}}$. Consider a vector [c], whose elements are $c_m = \sqrt{\tilde{Q}_{mm}}$, $m = 1, \ldots, M$, and the matrix $[C] = [c][c]^T$, so that $C_{mn} = \sqrt{\tilde{Q}_{mm}\tilde{Q}_{nn}}$. The on-diagonal elements of $[C]$ coincide with those of $\left[\tilde{Q}\right]$. $[C]$ is positive semi-definite with $M-1$ zero eigenvalues [48, p. 54]. The non-zero eigenvalue is the trace of $\left[\tilde{Q}\right]$. Therefore, $[C]$ is a suitable $\left[\tilde{Q}\right]$ matrix, i.e. the desired condition for $\nu_{\max}$ close to $T_{\tilde{Q}}$ is given by Equation (24). However, the bound cannot be attained because $[\tilde{Q}]$ is positive-definite.